catalysts

MDPI

Article

Facile Synthesis of Amorphous $C_3N_4Zn_xO_y$ (x, y = 0.32–1.10) with High Photocatalytic Efficiency for Antibiotic Degradation

Ran Zhang, Jing Xian Dong, Guo Liang Gao, Xue Lu Wang * and Ye-Feng Yao *

Physics Department & Shanghai Key Laboratory of Magnetic Resonance,
School of Physics and Electronic Science, East China Normal University, North Zhongshan Road 3663, Shanghai 200062, China; zhangran1323@163.com (R.Z.); dongjingxian10@163.com (J.X.D.); guoliang501@163.com (G.L.G.)

* Correspondence: xlwang@phy.ecnu.edu.cn (X.L.W.); yfyao@phy.ecnu.edu.cn (Y.-F.Y.); Tel.: +86-21-62234328 (Y.-F.Y.)

Received: 30 March 2020; Accepted: 5 May 2020; Published: 7 May 2020

Abstract: The development of novel, noble metal-free semiconductor catalysts with high efficiency is of great importance for the degradation of organic compounds. Among them, amorphous materials have been extensively studied for their unique and commercially useful properties. Here, a completely amorphous, noble metal-free photocatalyst $C_3N_4Zn_xO_y$ (x, y = 0.32–1.10) was successfully synthesized from urea and ZnO by a simple high-temperature polymerization method. As the Zn content increased, the short-range ordered structures of the amorphous samples were still retained, as revealed by XPS, FTIR, and ssNMR. Meanwhile, the -CN_3 structures were observed to be gradually destroyed, which may make the amorphous state more favorable for photocatalytic reactions. Compared with g-C_3N_4, the amorphous samples showed significantly reduced intensities in the photoluminescence spectra, indicating that the recombination rate of the photo-generated charge carriers was greatly reduced. It was confirmed that the optimized sample ($C_3N_4Zn_{0.61}O_{0.61}$) achieved a photocatalytic efficiency of 86.1% in the degradation of tetracycline hydrochloride under visible light irradiation within 1 h. This is about 2 times higher than that of both g-C_3N_4 and ZnO. This study emphasizes the importance of the amorphous structure in photocatalytic reactions, and this synthetic strategy may provide an effective model for designing other novel catalysts.

Keywords: amorphous; photocatalyst; photocatalytic reaction; tetracycline; degradation

1. Introduction

The discovery and application of antibiotics is a revolution in human history. Due to the prominent antibacterial and bactericidal effects, antibiotics have a high consumption rate in humans and livestock medicines. Tetracycline (TC), one of the most widely used antibiotics in the world, plays an important role in the medical industry due to its broad-spectrum antimicrobial effect on a variety of diseases [1,2]. However, the large amount of antibiotic residues discharged into wastewater poses a serious threat to ecosystems [3–5]. The most appropriate and effective method to effectively eliminate antibiotics from the environment has become a public issue in the international community. At present, several techniques have been developed to remove antibiotic residues such as activated carbon adsorption, UV/H_2O_2 processes, ozone oxidation, biodegradation, and electrolysis [6–9]. Recently, photocatalytic degradation based on semiconductors has been considered one of the most promising approaches, owing to the green byproduct and high efficiency compared with other traditional techniques [10,11].

Over the past few years, while most photocatalysts are based on crystalline compounds, a growing class of amorphous materials has shown higher efficiency than their crystalline counterparts. Amorphous materials have attracted much attention due to their unique isotropic and high concentration

of coordinatively unsaturated sites. The long-range disorder but short-range order in these structures provide more active and selective sites that exhibit excellent activity and selectivity in photocatalytic reactions [12–19]. Moreover, the amorphous nanostructures not only improve the adsorption capacity of the catalyst but also increase the contact area between the adsorbate and the catalyst. It is reported that amorphous metal sulfides (e.g., MoS_x and CoS_x) exhibit excellent performance in the hydrogen evolution reaction (HER) [16,17,20], while amorphous metal oxides (e.g., MO_x, M = Fe, Co, and Ni) are highly efficient in the oxygen evolution reaction (OER) [21–25]. Recent studies also showed that amorphous TiO_2 and amorphous g-C_3N_4 exhibit enhanced photocatalytic activities in hydrogen generation [26–30] and pollution degradation [31]. Although some progress has been made in studying the catalytic properties of photocatalysts, it is still necessary to design novel materials and gain a deep understanding of their catalytic mechanisms.

Herein, a completely amorphous material, which is denoted as $C_3N_4Zn_xO_y$ (x, y = 0.32–1.10), was successfully fabricated by a simple one-step thermal polymerization method. As the Zn content increased, the regions of crystallization were destroyed and became amorphous. ^{13}C ssNMR spectra revealed that the heptazine carbon (-CN_3) functional group in the sample gradually disappeared. The increase in the Zn element leads to an increase in the band gap and a decrease in the specific surface area, but the $C_3N_4Zn_xO_y$ samples show enhanced photocatalytic activity compared to g-C_3N_4 and ZnO. The optimized sample ($C_3N_4Zn_{0.61}O_{0.61}$) achieved a photocatalytic efficiency of 86.1% in the degradation of tetracycline hydrochloride (TC-HCl) under visible light irradiation (0.6 W/cm^2) within 1 h, which was about 2 times higher than that of both pure g-C_3N_4 and ZnO.

2. Results and Discussion

2.1. Element Analysis

Table 1 shows the H, C, N, and O elemental analysis results of the as-prepared samples, and the percentage of the Zn element was calculated based on the total mass proportion. The C/N atomic ratio of g-C_3N_4 is 2.7:4, which is close to 3:4. As for the other four samples, the C/N ratio did not change significantly from 2.7:4. For simplicity, the samples were designated $C_3N_4Zn_xO_y$ (x, y = 0.32–1.52), where x and y represent the number of Zn and O atoms relative to the N atom, respectively. It is worth noting that a small amount of oxygen resided in g-C_3N_4 which is attributed to the oxygenated carbon (C=O) because of the incomplete polymerization during the formation of g-C_3N_4. The addition of Zn caused a change in the oxygen content, which may be due to changes in the configurations of the oxygen combination binding sites. The specific surface areas of g-C_3N_4 and $C_3N_4Zn_xO_y$ samples were measured by monitoring nitrogen adsorption–desorption isotherms, as shown in Figure S1. The g-C_3N_4 and ZnO samples possessed a specific surface area of 89.8 and 29.9 m^2 g^{-1}, respectively, while the specific surface areas of the $C_3N_4Zn_xO_y$ samples were between the above two. The higher the Zn content, the smaller the specific surface area.

Table 1. Elemental analysis and specific surface areas of g-C_3N_4 and $C_3N_4Zn_xO_y$ (x, y = 0.32–1.52) samples.

Sample	H (wt %)	C (wt %)	N (wt %)	O (wt %)	Zn (wt %)	Atom Ratio (C:N:O:Zn)	Specific Surface Area (m^2/g)
g-C_3N_4	1.94	34.60	59.86	4.23	0	2.70:4:0.25:0.00	89.8
$C_3N_4Zn_{0.32}O_{0.51}$	1.35	27.41	46.82	6.83	17.60	2.73:4:0.51:0.32	75.5
$C_3N_4Zn_{0.61}O_{0.61}$	0.98	23.21	40.24	7.06	28.52	2.69:4:0.61:0.61	45.9
$C_3N_4Zn_{1.10}O_{1.02}$	0.80	17.69	31.72	9.28	40.52	2.60:4:1.02:1.10	42.7
$C_3N_4Zn_{1.52}O_{1.30}$	0.55	16.07	26.53	9.86	47.00	2.83:4:1.30:1.52	41.5

2.2. X-Ray Diffraction

The phase structures of the as-prepared catalysts were examined by X-ray diffraction (XRD). As shown in Figure 1a, pure g-C_3N_4 exhibited two diffraction peaks at 12.9° and 27.3°, representing

the (100) and (002) crystal faces, respectively. The peak at 12.9° represents the in-plane repeating tri-s-triazine ring structure, and the peak at 27.3° originates from the interlayer stacking of the π-conjugated aromatic system. As the Zn content increased, the peaks at both sites gradually weakened and slowly disappeared. The scattering curves show a large broad baseline with no obvious peak, indicating an amorphous structure. When the mass ratio of urea/ZnO is in the range of 25–100, a completely amorphous sample $C_3N_4Zn_xO_y$ (x, y = 0.32–1.10) can be obtained. The disappearance of the diffraction peaks also demonstrates that the arrangement of the repeating unit structures of g-C_3N_4 may be damaged to a short-range order. When the Zn content continuously increases, peaks gradually arise at 32°, 34.6°, 36.4°, 47.7°, 56.7°, 63° and 68.1° of the $C_3N_4Zn_{1.52}O_{1.30}$ sample, which correspond to the ZnO diffraction peaks.

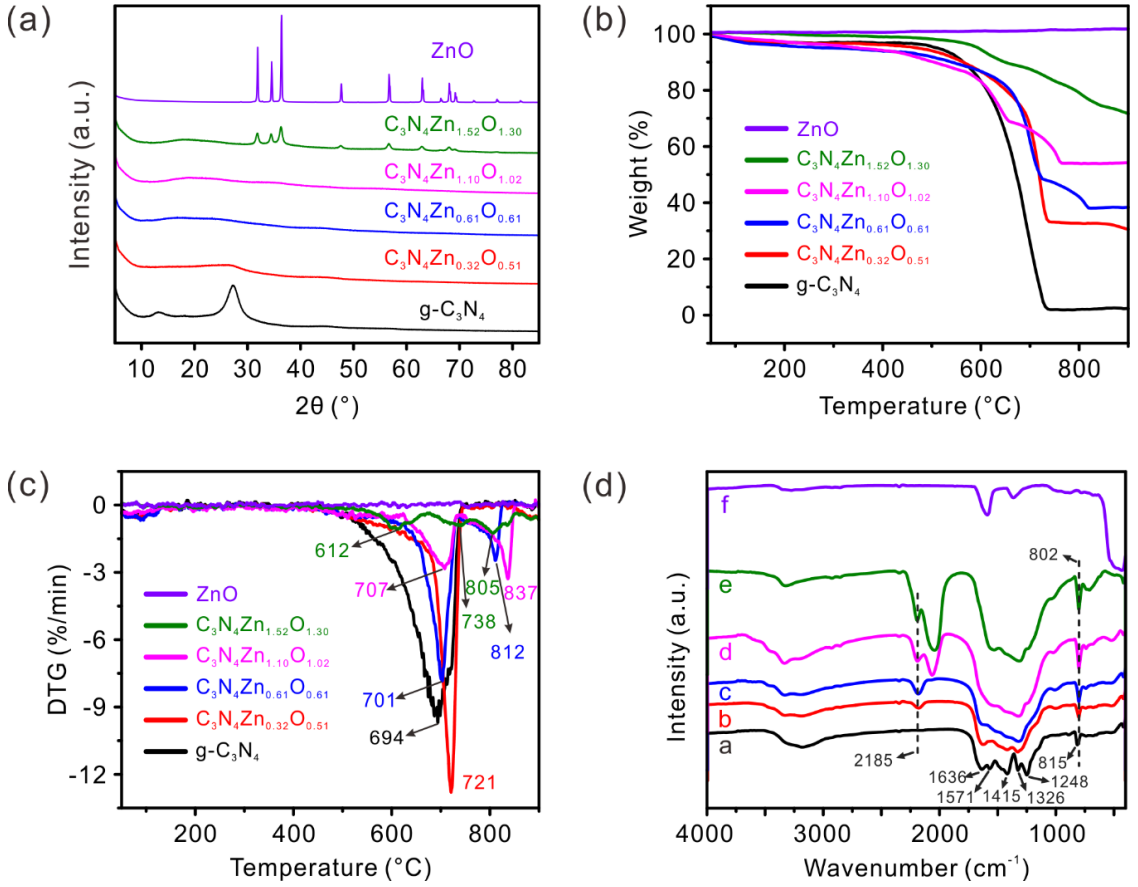

Figure 1. (**a**) XRD patterns, (**b**) Thermogravimetric analysis (TGA) curves, and (**c**) DTG curves of g-C_3N_4, $C_3N_4Zn_xO_y$, and ZnO samples. (**d**) Fourier transform infrared spectra (FTIR) of (a) g-C_3N_4, (b) $C_3N_4Zn_{0.32}O_{0.51}$, (c) $C_3N_4Zn_{0.61}O_{0.61}$, (d) $C_3N_4Zn_{1.10}O_{1.02}$, (e) $C_3N_4Zn_{1.52}O_{1.30}$ and (f) ZnO. Recorded in transmission mode.

2.3. Thermogravimetric Analysis

To better understand the effect of the raw material ratio on the decomposition of the final product produced by the pyrolysis process, thermogravimetric analysis (TGA) was performed on g-C_3N_4, $C_3N_4Zn_xO_y$, and ZnO samples, as shown in Figure 1b. We also conducted the first derivative curve DTG in Figure 1c. From the TG and DTG curves, it can be found that ZnO maintains its mass during the heating process due to the high boiling point (2360 °C). The g-C_3N_4 and $C_3N_4Zn_xO_y$ samples are stable below 500 °C, and the mass gradually decreases in the range of 500–750 °C. It can be speculated that the C and N elements in these samples react with O_2 and volatilize. The most rapid mass loss occurs at about 700 °C, indicating the most intensive oxidation reaction at this temperature. It should

be noted that a second decrease appears at about 810 °C in the $C_3N_4Zn_{0.61}O_{0.61}$, $C_3N_4Zn_{1.10}O_{1.02}$, and $C_3N_4Zn_{1.52}O_{1.30}$ samples. This indicates that partial C and N elements may have formed strong covalent bonds in these samples, such as C≡N or Zn–N, therefore a higher temperature may be needed to cause the formation of CO_2, NO, etc. It is assumed that the formation of new strong covalent bonds leads to the destruction of the long-range ordered structure, thus no diffraction peaks can be seen in the XRD spectra of the $C_3N_4Zn_xO_y$ samples.

2.4. FTIR Spectra

In the FTIR spectrum (Figure 1d) of ZnO, the peaks around 500 cm^{-1} correspond to the characteristic Zn–O stretching vibration modes. The FTIR spectrum of g-C_3N_4 shows the apparent aromatic CN heterocycle stretching mode at 1200–1700 cm^{-1}. The bands appearing at 1248 cm^{-1}, 1326 cm^{-1}, and 1415 cm^{-1} are assigned to the aromatic C–N vibrations in the structure. The peaks at 1571 cm^{-1} and 1636 cm^{-1} correspond to C=N stretching modes of the aromatic ring in the g-C_3N_4 structure. The band near 815 cm^{-1} is attributed to the out of plane bending modes of C–N heterocycles, which can be considered as the main peak reflecting the existence of the g-C_3N_4 structure. As for the $C_3N_4Zn_xO_y$ samples, all of the FTIR spectra are similar with a sharp band at 802 cm^{-1} and stretching bands around 1200–1700 cm^{-1}, indicating that the C–N heterocycles are maintained and the short-range order of g-C_3N_4 remains unchanged. It should be noted that the band at 815 cm^{-1} was slightly shifted to 802 cm^{-1}, which may due to the transfer of interfacial charge and the formation of new chemical bonds [32]. The peak at 2185 cm^{-1}, which can be assigned to C≡N triple bonds [33,34], only appeared in the $C_3N_4Zn_xO_y$ samples. The peak intensity increased with the ZnO content, indicating that some triazine rings were broken and the sp^2 C–N bonds were transformed into C≡N triple bonds. The above behaviors exist in the g-C_3N_4/ZnO composite, indicating that the $C_3N_4Zn_xO_y$ samples have a lot of similarities with the g-C_3N_4/ZnO composite. In addition, this is well in line with the DTG results.

2.5. SEM Images

The morphologies of g-C_3N_4, $C_3N_4Zn_xO_y$, and ZnO samples were assessed by SEM images (Figure 2), revealing differences in their structure. Pure g-C_3N_4 exhibited a wrinkled and folded thin-sheet morphology (Figure S2). As the Zn content increased, the $C_3N_4Zn_xO_y$ samples gradually became a denser layered structure and finally transformed into a large lamellar structure. The corresponding EDS mapping revealed that the Zn and O elements were dispersed uniformly in $C_3N_4Zn_{1.10}O_{1.02}$. The EDS mapping of the other samples is shown in Figure S3.

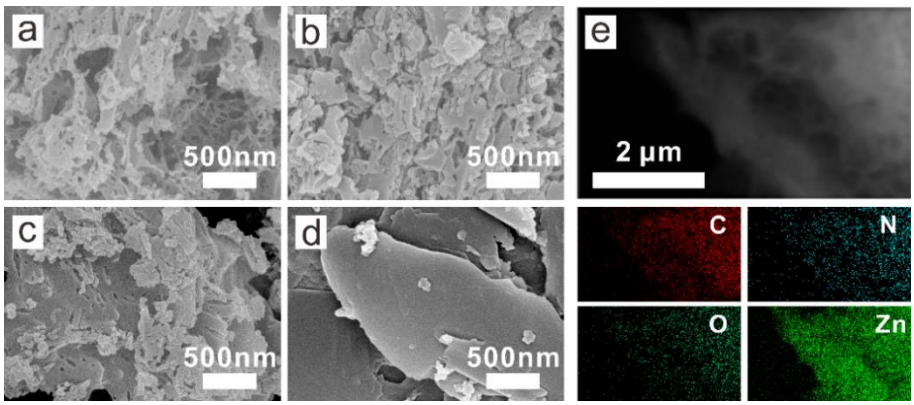

Figure 2. SEM images of (**a**) $C_3N_4Zn_{0.32}O_{0.51}$, (**b**) $C_3N_4Zn_{0.61}O_{0.61}$, (**c**) $C_3N_4Zn_{1.10}O_{1.02}$ and (**d**) $C_3N_4Zn_{1.52}O_{1.30}$; (**e**) EDS mapping of $C_3N_4Zn_{1.10}O_{1.02}$.

2.6. Optical Band Gap Measurement

The optical properties of the as-prepared samples were characterized by UV-Vis diffuse reflectance spectroscopy. As shown in Figure 3a, pure g-C_3N_4 displayed an absorption band below 450 nm, whereas the $C_3N_4Zn_xO_y$ samples exhibited an onset of absorbance farther out in the visible region and below 600 nm. The band gaps of the samples were obtained based on the Tauc plot, as shown in Figure 3b. Compared with g-C_3N_4, the band gaps of the $C_3N_4Zn_xO_y$ samples first decreased upon introducing small quantities of ZnO into urea, and then, rose to near the band gap of ZnO upon increasing the ZnO content. The conduction bands of these photocatalysts were estimated using the valence band X-ray photoelectron spectra (VBXPS), as shown in Figure S4. The relative positions of valence and conduction band energies are depicted in Figure S5.

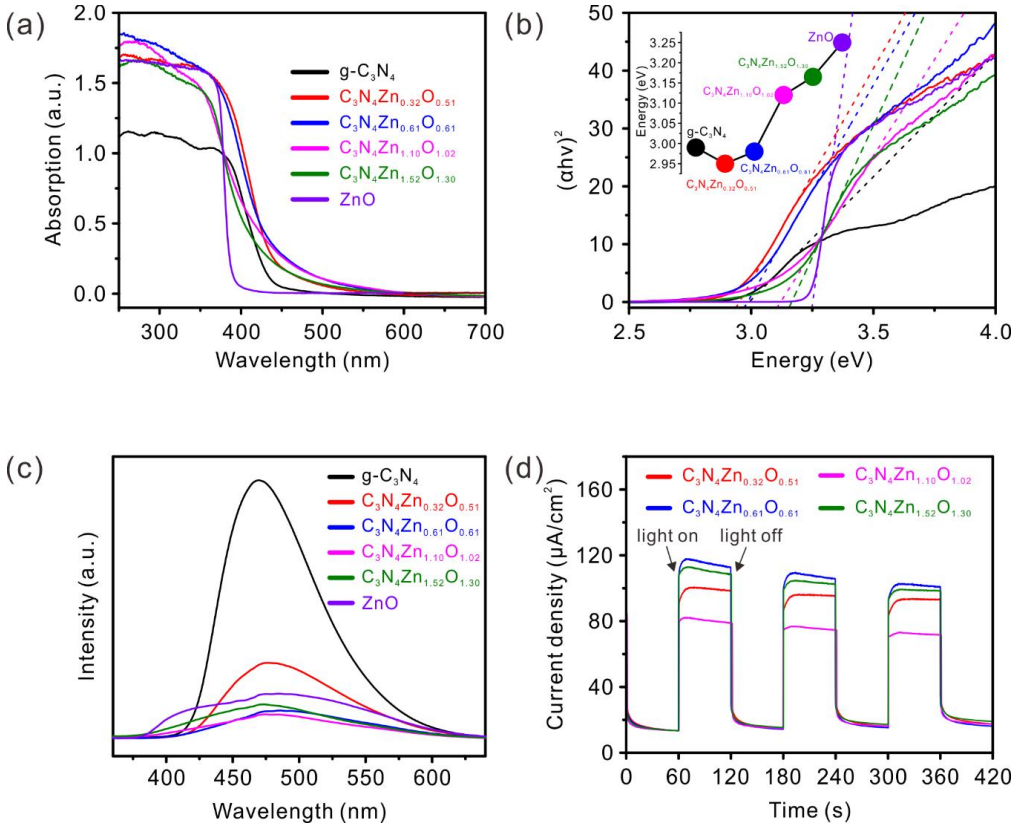

Figure 3. (**a**) UV-Vis absorption spectra of g-C_3N_4, $C_3N_4Zn_xO_y$, and ZnO samples. (**b**) Tauc plot of g-C_3N_4, $C_3N_4Zn_xO_y$, and ZnO samples, appropriate for evaluating optical band gap energies of indirectly allowed transitions. (**c**) Photoluminescence emission spectra of g-C_3N_4, $C_3N_4Zn_xO_y$, and ZnO at the excitation wavelength of 325 nm. (**d**) Transient photocurrent generation from $C_3N_4Zn_xO_y$ electrodes at 0.6 V versus Ag/AgCl in 0.2 M Na_2SO_4 plus 10 vol% triethanolamine (TEOA) under a 300 W xenon lamp full spectrum irradiation (320–780 nm, 0.8 W/cm^2).

2.7. Photoluminescence and Photocurrent Measurements

The room temperature photoluminescence (PL) spectra of g-C_3N_4, $C_3N_4Zn_xO_y$, and ZnO photocatalysts are plotted in Figure 3c. Each spectrum consists of one broad band around 470 nm in the visible region. Compared to g-C_3N_4, the PL intensities of the $C_3N_4Zn_xO_y$ samples all decreased, which indicates that the photo-generated electron-hole recombination is much more inhibited. The lowest PL intensity of $C_3N_4Zn_{1.10}O_{1.02}$ indicates the lowest recombination rate among the $C_3N_4Zn_xO_y$ samples.

Transient photocurrent responses of the $C_3N_4Zn_xO_y$ samples were investigated at a constant voltage of 0.6V versus Ag/AgCl, with several on–off cycles of intermittent full wavelength irradiation (320–780 nm, 0.8 W/cm^2). As shown in Figure 3d, all samples exhibit stable and high-speed current

swings during the illumination cycle, thus demonstrating rapid and steady photoelectrochemical efficiency. The $C_3N_4Zn_{0.61}O_{0.61}$ sample exhibits a significantly higher photocurrent intensity than the other three samples.

2.8. X-Ray Photoelectron Spectroscopy (XPS)

To further investigate the surface composition of $C_3N_4Zn_xO_y$ and the change in the chemical states of the C, N, O, and Zn elements, XPS analysis was carried out. Figure 4 shows the XPS spectra arising from the C 1s, N 1s, O 1s, and Zn 2p photoelectrons obtained from the samples of g-C_3N_4, $C_3N_4Zn_xO_y$, and ZnO. Two peaks were observed in the XPS spectra of C 1s for g-C_3N_4; the peak with a binding energy of 288.7 eV corresponds to the N–C=N repeat unit of g-C_3N_4, while the second C peak at 284.6 eV originates from sp^2 orbitals in C=C bonds [35]. For the $C_3N_4Zn_xO_y$ samples, the existence of the peak at 288.7 eV indicates that the N–C=N functional group remains. The N 1s XPS spectrum for g-C_3N_4 exhibits three peaks at 399.18 eV, 400.43 eV, and 401.62 eV, which are assigned to the C–N=C repeat unit, N-$(C)_3$ and NH_x groups, respectively (Figure 4 N 1s) [35]. The N 1s spectra from $C_3N_4Zn_xO_y$ samples exhibit some differences based on ZnO content. With the increase in the Zn constituent, the peaks at 401.62 eV disappear, indicating the absence of the NH_x group. It is speculated that the N atom of the NH_x group may be connected to the Zn atom instead.

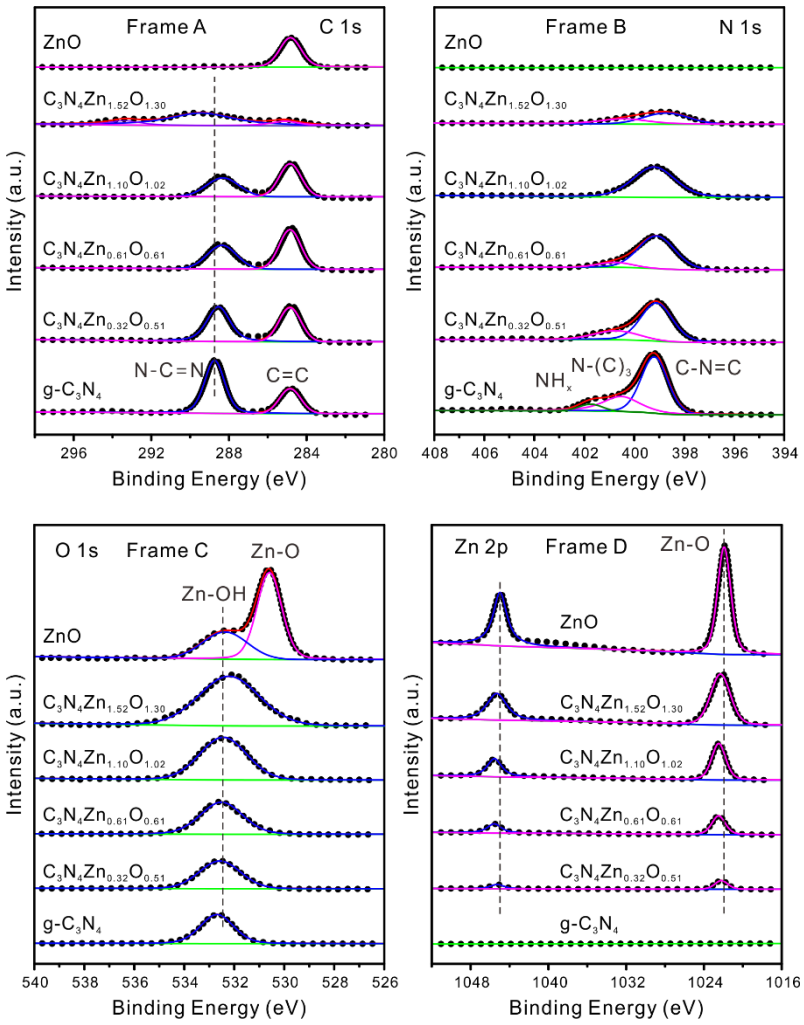

Figure 4. XPS spectra of g-C_3N_4, $C_3N_4Zn_xO_y$, and ZnO samples. Frame A: C 1s photoelectron energies; Frame B: N 1s photoelectron energies; Frame C: O 1s photoelectron energies; Frame D: Zn 2p photoelectron energies.

The O 1s spectra for ZnO display two peaks at 530.68 eV and 532.55 eV (Figure 4 O 1s). The peak at 530.32 eV represents the electron binding energy in the Zn–O bond, corresponding to the O^{2-} ions that are surrounded by Zn^{2+} ions. The peak at 532.55 eV derives from Zn–OH or loosely bound oxygen, such as -CO_3, -OH, adsorbed H_2O, and O_2 [36–40]. The XPS spectra of O 1s from the $C_3N_4Zn_xO_y$ samples all show only one peak at 532.55 eV. It is suspected that the O element exists in the form of Zn–OH in the $C_3N_4Zn_xO_y$ samples. With the decrease in the Zn and O content, the peak at 532.55 eV slightly shifted to higher binding energy, which may due to the change in the migration of electrons and causes the formation of N–Zn–O covalent bonds [41]. The XPS spectra of Zn 2p for ZnO show two symmetry peaks at 1044.98 eV and 1021.88 eV (Figure 4 Zn 2p). These are attributed to the Zn $2p_{1/2}$ and Zn $2p_{3/2}$ orbitals, respectively, indicating that the Zn element exists in the form of Zn^{2+} [36,37,39] The XPS spectra of Zn 2p for the $C_3N_4Zn_xO_y$ samples exhibit no significant change with increasing ZnO content except for a small shift, which can be attributed to the formation of N–Zn bonds [42]. The slight peak shifts in O 1s and Zn 2p spectra exist in the g-C_3N_4/ZnO composite, which demonstrates that the $C_3N_4Zn_xO_y$ samples and the g-C_3N_4/ZnO composite have a lot in common.

2.9. ^1H and ^{13}C NMR Spectra

In addition to XPS, solid-state NMR is an important method for structural characterization. As shown in Figure 5, two peaks were observed in the ^1H spectrum of g-C_3N_4, which are assigned to the edge-NH_2 groups (8.7 ppm) and water (3.8 ppm), respectively [43]. As the Zn content increases, the peak at 8.7 ppm gradually disappears, which demonstrates that the edge-NH_2 groups vanish in $C_3N_4Zn_xO_y$ samples. At the same time, a new peak at 0.7 ppm gradually increases. We assign this peak to the Zn–OH group. The ^{13}C spectrum of g-C_3N_4 also exhibits two peaks at 156.8 and 164.9 ppm that represent the C atoms in melem-CN_3 and the C atoms connected to the edge -NH_x group (-CN_2–NH_x) [43]. The peak at 156.8 ppm gradually disappears with an increase in the Zn content, indicating the -CN_3 structure gradually disintegrates. The full width at half maxima (FWHM) of the peak at 164.9 ppm becomes broader, which may be related to the changes in the edge -NH_x group. An appropriate explanation is that the edge N is connected to Zn to form a -CN_2–N–Zn structure. This is well in line with the observations in the XPS experiments.

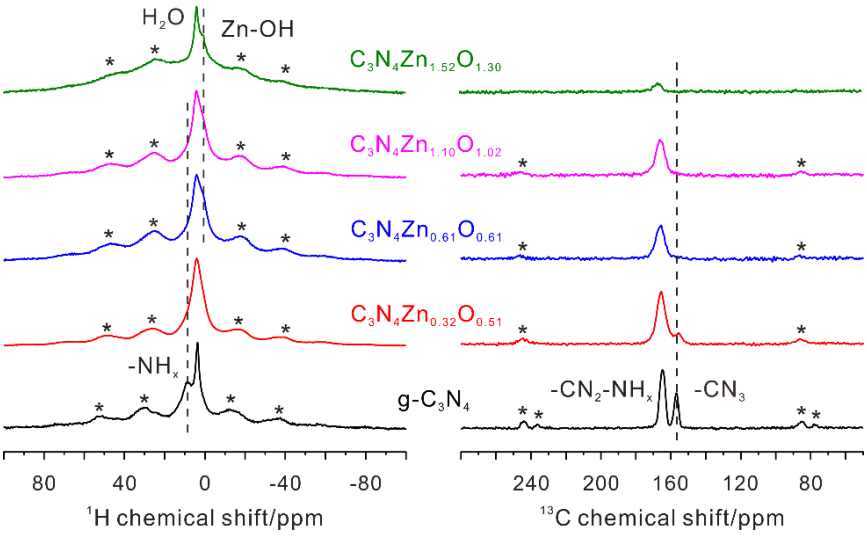

Figure 5. ^1H and ^{13}C NMR spectra of g-C_3N_4, $C_3N_4Zn_xO_y$, and ZnO samples. The spectra were obtained at a MAS spinning rate of 8 kHz and the symbol * represents the spinning sidebands. The chemical shifts of the spectra were calibrated according to adamantane (^1H 1.46 ppm, ^{13}C 38.56 ppm).

2.10. Photodegradation of Tetracycline

Tetracycline represents a major fraction of the current antibiotic market worldwide, and tetracycline hydrochloride (TC-HCl) was selected as a representative pollutant-toxin to evaluate the photocatalytic performance of the $C_3N_4Zn_xO_y$ in detoxification. Figure 6a shows the UV-Vis absorption spectra of TC-HCl at different irradiation times by using $C_3N_4Zn_{0.61}O_{0.61}$ as the photocatalyst. It can be found that the maximum absorption peak of the TC-HCl solution is at 365 nm. After 0.5 h absorption in the dark, the peak shifts to 372 nm. When the visible light ($\lambda > 420$ nm) is on, the TC-HCl degrades rapidly in the first hour, after which the rate slows down. Figure 6b shows the photocatalytic activities of g-C_3N_4, $C_3N_4Zn_xO_y$, and ZnO samples in the degradation of TC-HCl under constantly visible light irradiation. The blank sample represents the direct photolysis of TC-HCl in the absence of the photocatalyst and under visible light irradiation for 2 h. TC-HCl was only slightly degraded under such conditions, demonstrating that TC-HCl is stable under visible light irradiation when there is no photocatalyst involved. Pure g-C_3N_4 and ZnO showed good performance in the degradation of TC-HCl, and pure g-C_3N_4 exhibited a relatively higher degradation rate than ZnO because it has a better absorption to visible light. Significantly, the $C_3N_4Zn_xO_y$ (x, y = 0.32–1.52) photocatalysts samples exhibited much higher activities for photodegrading TC-HCl than either pure g-C_3N_4 or ZnO. With the addition of the Zn and O element in the composites, the photocatalytic activity of $C_3N_4Zn_xO_y$ (x, y = 0.32–1.52) increased remarkably. The $C_3N_4Zn_{0.61}O_{0.61}$ sample exhibited the highest photocatalytic activity, which can degrade TC-HCl by 86.1% in 1 h, and 92.7% in 2 h. It should be noticed that the degradation curve of $C_3N_4Zn_{0.32}O_{0.51}$ had a very fast response, especially in the first 0.5 h, but the final degradation rate was lower than $C_3N_4Zn_{0.61}O_{0.61}$ within 2 h. After 0.5 h, the concentration of the TC-HCl solution was basically unchanged. This may due to the competition between TC-HCl and the intermediate degradation products; it is related to the reactive oxygen species (ROS) formed by the catalyst [44]. As far as we know, the ROS includes singlet oxygen ($^1O_2$), hydroxyl radicals (•OH), superoxide anions ($•O^{2-}$), etc., [45]. Previous researchers have reported that •OH or/and $•O^{2-}$ radicals play important roles in the photodegradation of tetracycline by the g-C_3N_4/ZnO composite [46,47]. Since the $C_3N_4Zn_xO_y$ samples have many similarities with g-C_3N_4/ZnO, it is suspected that •OH or/and $•O^{2-}$ radicals induced by light irradiation of the $C_3N_4Zn_xO_y$ samples also control the degradation rate of TC-HCl. As the degradation reaction proceeds, the concentration of the intermediates gradually increases. The further reaction of the intermediates would cause the •OH and $•O^{2-}$ radicals to be consumed. Therefore, the degradation rate of TC-HCl will be reduced. In general, the results indicate that the $C_3N_4Zn_xO_y$ photocatalysts have a better performance in the photodegradation of organic pollutants than either the pristine g-C_3N_4 or ZnO under the same conditions, especially the completely amorphous $C_3N_4Zn_xO_y$ (x, y = 0.32–1.10) samples.

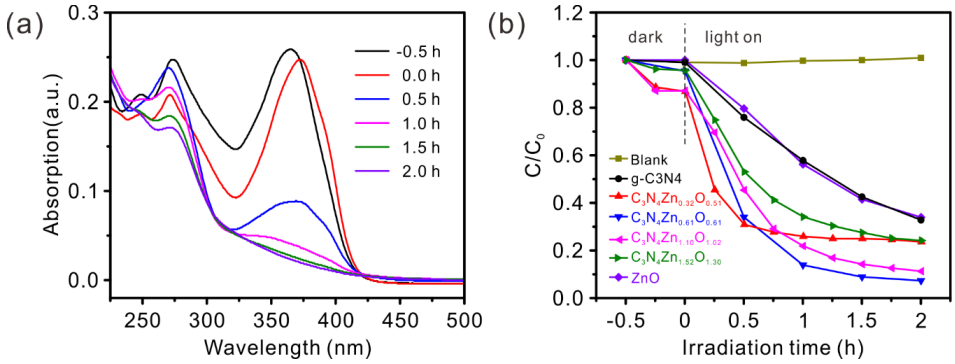

Figure 6. (**a**) The absorption spectra of TC-HCl solution (10 mg/L) at different irradiation times under visible light, using $C_3N_4Zn_{0.61}O_{0.61}$ as the photocatalyst. (**b**) Photocatalytic degradation efficiencies of TC-HCl using g-C_3N_4, $C_3N_4Zn_xO_y$, and ZnO as the photocatalysts under visible light irradiation (420–780 nm, 0.6 W/cm^2).

The reusability of the $C_3N_4Zn_{0.61}O_{0.61}$ sample was further studied. The sample powders were collected by filtration after photocatalytic reactions and reused in the photocatalytic reaction for 3 times under the same conditions. As shown in Figure 7, the $C_3N_4Zn_{0.61}O_{0.61}$ sample displays good stability and maintains a high photocatalytic performance during three reaction cycles. The gradual decrease in the photocatalytic performance may be due to the mass loss during the sampling, transferring, and filtration processes. A 50 mg sample was used in the first reaction cycle. The final powder catalyst was filtered and dried after three reaction cycles, and only about 10 mg of the sample was obtained. This indicates that the powder lost a lot when conducting the next reaction cycle. Similar results have been reported previously [48].

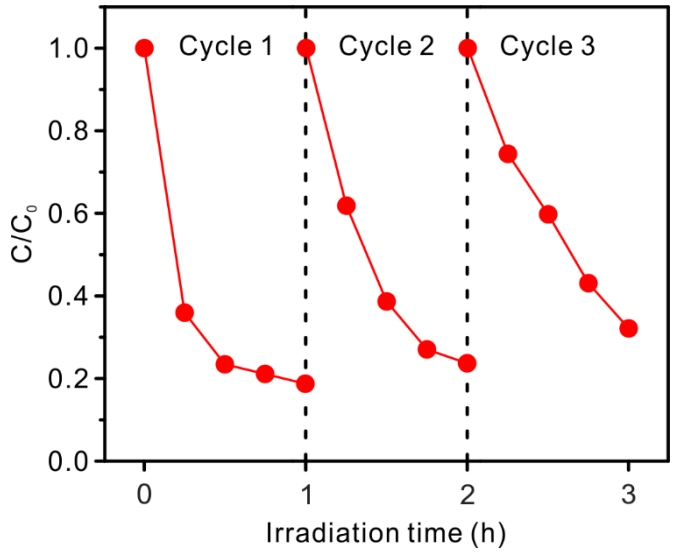

Figure 7. Recycling properties of the $C_3N_4Zn_{0.61}O_{0.61}$ photocatalyst.

We conducted SEM and EDS tests on the $C_3N_4Zn_{0.61}O_{0.61}$ sample before and after the photocatalytic degradation of TC-HCl. The SEM image of the $C_3N_4Zn_{0.61}O_{0.61}$ sample exhibits a dense layered structure (Figure S6a). After the degradation of TC-HCl for 1 h under light irradiation, the morphology of the sample did not change much (Figure S6b). The EDS was also employed to better understand the surface element composition and the content of the $C_3N_4Zn_{0.61}O_{0.61}$ sample before and after photocatalytic degradation. The SEM images and the corresponding EDS were shown in Figure S7. From the EDS in Figure S7c, it can be known that the surface of the $C_3N_4Zn_{0.61}O_{0.61}$ sample contains C, N, O, and Zn elements. After degrading TC-HCl for 1 h under visible light irradiation, the surface element composition is the same as before (Figure S7d). The element contents are depicted in both spectra, from which we can know that the content of each element on the surface of the $C_3N_4Zn_{0.61}O_{0.61}$ sample only changed slightly after the degradation experiment. To be more specific, the mass portion of the Zn element changed from 43.05% to 41.55%, but the C and N elements on the surface of the sample also changed slightly. The C/N mass ratio changed from 1.39 to 1.33, indicating that a small amount of C or N elements were lost after the degradation. Therefore, the loss of trace Zn elements in the reaction will be accompanied by the trace loss of C or N elements. Based on the EDS results, the difference in the Zn element before and after degradation is about 1.5%. The initial weight of the $C_3N_4Zn_{0.61}O_{0.61}$ sample is 50 mg, and the leaching of Zn into the solution should be 0.75 mg. For a 200 mL solution, the concentration of Zn would be 3.75 mg/L. In the practical experiment, the final volume of the TC-HCl solution is less than 200 mL due to the sampling process. Therefore, the concentration of Zn would be lower than 3.75 mg/L.

To our knowledge, the photoactivity of the commercial ZnO can be seriously deteriorated due to the photocorrosion effect [49,50]. It is reported that 92 % of MB could be degraded within 2 h when ZnO was used for the first time; however, after three recycles, a significant decrease in photocatalytic

activity for pure ZnO was found, in which only 16% of MB was degraded [51]. The drastic decrease was explained as the photocorrosion effect. Photocorrosion consists of the partial dissolution of Zn and the collapse of the ZnO structure induced by the light irradiation [52,53]. That is to say, partial Zn elements may get into the solution. In our work, the $C_3N_4Zn_xO_y$ samples were fabricated from commercial ZnO. It has been revealed that the Zn–O functional group exists in the $C_3N_4Zn_xO_y$ samples. Therefore, photocorrosion cannot be completely absent. Fortunately, the $C_3N_4Zn_{0.61}O_{0.61}$ sample is still highly efficient after being reused to degrade TC-HCl, as shown in Figure 7. This indicates that the $C_3N_4Zn_{0.61}O_{0.61}$ sample has good stability and photocorrosion has been inhibited.

3. Materials and Methods

3.1. Sample Preparation

The samples were synthesized by a one-step polymerization method according to the literature [54]. In brief, 2.0 g urea (≥98%, Sigma-Aldrich, St. Louis, MO, USA) and a certain amount (0.02, 0.05, 0.08 or 0.20 g) of ZnO (≥99%, Sigma-Aldrich, St. Louis, MO, USA) were mixed in a covered alumina crucible, then, the powders were transferred to a muffle furnace and calcined at 500 °C for 2 h with a heating rate of 10 °/min under air atmosphere. The samples were obtained after cooling to room temperature.

3.2. Material Characterization

The nanoparticle phase and structural information of the as-prepared materials were characterized by X-ray powder diffraction (XRD) measurements. The data were recorded in the 2θ angle range of 5° to 85° with a scan speed of 10°/min on an Ultima IV (Rigaku, Japan) X-ray diffractometer with Cu-Kα radiation (λ = 1.5418 Å, 35 kV, 25 mA). The surface morphologies were obtained using a scanning electron microscope (Hitachi S-4800, Japan). Thermal gravimetric (TG) curves were recorded using an STA 449 F3 Jupiter simultaneous thermo-analyzer (NETZSCH Gerätebau GmbH, Germany) from room temperature to 900 °C with a heating rate of 10 °C/min under air atmosphere. The specific surface properties of the powder samples were obtained by nitrogen adsorption–desorption isotherms, using an ASAP 2020 physical adsorption analyzer (Micromeritics, USA). The specific surface areas were obtained based on the BET equation. The elemental composition and content were characterized by an EA analyzer (Elementar Vario EL cube, Germany). The optical properties were measured by a UV-Vis spectrophotometer (UV-2700, Shimadzu, Japan) at a wavelength range of 200–800 nm. The X-ray photoelectron spectroscopy (XPS) data were recorded using an Escalab 250Xi (Thermo Scientific, USA). All binding energies were calibrated to the C 1s peak at 284.6 eV. The structural information of the powders was analyzed by an AVANCE III 400 NMR spectrometer (Bruker, German), operating at a ^{1}H Larmor frequency of 400 MHz. The ^{1}H spectra have a spectral width of 200 ppm, 90° pulse width of 4 μs, acquisition time of 10 ms, number of scans of 16, and recycle delay of 2 s. The ^{13}C spectra have a spectral width of 300 ppm, 90° pulse width of 4 μs, acquisition time of 20 ms, number of scans of 4 k, and recycle delay of 2 s. A Nexus 670 infrared spectrometer (Nicolet, USA) was used to perform Fourier transform infrared spectroscopy (FTIR) analysis in the wavenumber range of 4000–400 cm^{-1} in transmission mode. The photoluminescence (PL) spectra within the wavelength range of 350–700 nm were obtained under 325 nm excitation using an F-4500 FL spectrophotometer (Hitachi, Japan).

The photoelectrochemical test was conducted with an electrochemical workstation (CHI660E Instruments, Shanghai, China) in a standard three-electrode cell with 0.2 M Na_2SO_4 plus 10 vol % triethanolamine (TEOA). The Pt gauze (1 × 1 cm^2) and Ag/AgCl (saturated KCl) was used as the counter electrode and reference electrode, respectively. The working electrode was prepared on an indium tin oxide (ITO) conductor glass. Precisely, 10 mg of the as-prepared photocatalyst, N, N-dimethylformamide (DMF, 200 μL), naphthol (50 μL) were blended and sonicated for 30 min to get a homogeneous mixture. Then, 20 μL of the slurry was then injected onto the ITO glass. The exposed area of the working electrode was 1 × 1 cm^2. The electrode was dried in air overnight to improve adhesion.

3.3. Photocatalytic Activity Tests

A 50 mg photocatalyst was dispersed in 200 mL tetracycline hydrochloride (TC-HCl) aqueous solution (10 mg/L). The mixed suspension was magnetically stirred for 30 min in the dark to obtain absorption–desorption equilibrium before irradiation. Afterwards, the above suspension was irradiated by a 300 W xenon lamp (PerfectLight, Beijing, China) with a 420 nm cutoff filter. The optical power density was measured to be 0.6 W/cm^2, using a PL-MW2000 optical power meter (PerfectLight, Beijing, China). At 15 min intervals, 4 mL of suspension was sampled and filtered through a 0.22 μm PTFE syringe filter to remove the solid particles and obtain a clear liquid. The photocatalytic degradation efficiency of TC-HCl was analyzed on a UV-Vis spectrophotometer (UV-2700, Shimadzu, Japan) by recording the absorption spectrum of the aqueous solution at the wavelength range of 200–500 nm.

4. Conclusions

A photocatalyst $C_3N_4Zn_xO_y$ (x, y = 0.32–1.10) synthesized by a calcining process from urea and ZnO precursors produced a completely amorphous product that was found to be useful for breaking down the aromatic compound tetracycline under visible light illumination. XRD, XPS, FTIR, ssNMR and other characterizations revealed that the as-prepared samples contained N–C=N structure, similar to that of g-C_3N_4. The starting Zn and O elements were believed to be disassembled and coordinated into a new C and N framework. The amorphous structures possess more defects and larger contact areas with reactants than either g-C_3N_4 or ZnO photocatalysts. This creates more effective active sites and better electron transfer efficiency. In the photocatalytic degradation of TC-HCl, the amorphous samples exhibited superior photocatalytic activities over pure g-C_3N_4 and ZnO. The new amorphous materials have potential applications in environmental pollution abatement and energy generation, and should provide a new direction for the development of photocatalytic materials in the future.

Supplementary Materials: The following are available online at http://www.mdpi.com/2073-4344/10/5/514/s1, Figure S1: Nitrogen adsorption–desorption isotherm curves of g-C_3N_4, $C_3N_4Zn_xO_y$, and ZnO samples. Inset: Calculated BET surface area per gram of sample. Figure S2: SEM images of (a) g-C_3N_4 and (b) ZnO. Figure S3: EDS mapping of (a) g-C_3N_4, (b) $C_3N_4Zn_{0.32}O_{0.51}$, (c) $C_3N_4Zn_{0.61}O_{0.61}$, (d) $C_3N_4Zn_{1.52}O_{1.30}$ and (e) ZnO. Figure S4: Valence band XPS spectra of (a) g-C_3N_4, (b) $C_3N_4Zn_{0.32}O_{0.51}$, (c) $C_3N_4Zn_{0.61}O_{0.61}$, (d) $C_3N_4Zn_{1.10}O_{1.02}$, (e) $C_3N_4Zn_{1.52}O_{1.30}$ and (f) ZnO. Figure S5: Band gap (a) g-C_3N_4, (b) $C_3N_4Zn_{0.32}O_{0.51}$, (c) $C_3N_4Zn_{0.61}O_{0.61}$, (d) $C_3N_4Zn_{1.10}O_{1.02}$, (e) $C_3N_4Zn_{1.52}O_{1.30}$ and (f) ZnO. Figure S6: SEM images of the $C_3N_4Zn_{0.61}O_{0.61}$ sample (a) before and (b) after the degradation of TC-HCl. Figure S7: SEM images of the $C_3N_4Zn_{0.61}O_{0.61}$ sample (a) before and (b) after the degradation of TC-HCl. EDS of the $C_3N_4Zn_{0.61}O_{0.61}$ sample (c) before and (d) after the degradation of TC-HCl.

Author Contributions: Methodology, software, validation, formal analysis, data curation, R.Z. and G.L.G.; Investigation, R.Z., G.L.G. and J.X.D.; writing—original draft preparation, R.Z.; conceptualization, resources, writing—review and editing, visualization, supervision, project administration, funding acquisition, X.L.W. and Y.-F.Y. All authors have read and agreed to the published version of the manuscript.

Funding: This research was funded by the National Natural Science Foundation of China, grant numbers 21603073 and 21574043.

Conflicts of Interest: The authors declare no conflict of interest.

References

1. Leong, S.; Li, D.; Hapgood, K.; Zhang, X.; Wang, H. Ni(OH)$_2$ decorated rutile TiO_2 for efficient removal of tetracycline from wastewater. *Appl. Catal. B Environ.* **2016**, *198*, 224–233. [CrossRef]
2. Zhang, J.; Yan, M.; Yuan, X.; Si, M.; Jiang, L.; Wu, Z.; Wang, H.; Zeng, G. Nitrogen doped carbon quantum dots mediated silver phosphate/bismuth vanadate Z-scheme photocatalyst for enhanced antibiotic degradation. *J. Colloid Interface Sci.* **2018**, *529*, 11–22. [CrossRef] [PubMed]
3. Hailili, R.; Wang, Z.-Q.; Li, Y.; Wang, Y.; Sharma, V.K.; Gong, X.-Q.; Wang, C. Oxygen vacancies induced visible-light photocatalytic activities of $CaCu_3Ti_4O_{12}$ with controllable morphologies for antibiotic degradation. *Appl. Catal. B Environ.* **2018**, *221*, 422–432. [CrossRef]

4. Pan, X.; Lv, N.; Li, C.; Ning, J.; Wang, T.; Wang, R.; Zhou, M.; Zhu, G. Impact of nano zero valent iron on tetracycline degradation and microbial community succession during anaerobic digestion. *Chem. Eng. J.* **2019**, *359*, 662–671. [CrossRef]
5. Wang, W.; Tadé, M.O.; Shao, Z. Research progress of perovskite materials in photocatalysis- and photovoltaics-related energy conversion and environmental treatment. *Chem. Soc. Rev.* **2015**, *44*, 5371–5408. [CrossRef]
6. Zhu, X.; Liu, Y.; Qian, F.; Zhou, C.; Zhang, S.; Chen, J. Preparation of magnetic porous carbon from waste hydrochar by simultaneous activation and magnetization for tetracycline removal. *Bioresour. Technol.* **2014**, *154*, 209–214. [CrossRef]
7. Kakavandi, B.; Takdastan, A.; Jaafarzadeh, N.; Azizi, M.; Mirzaei, A.; Azari, A.; Jaafarzadeh, N. Application of Fe_3O_4@C catalyzing heterogeneous UV-Fenton system for tetracycline removal with a focus on optimization by a response surface method. *J. Photochem. Photobiol. A Chem.* **2016**, *314*, 178–188. [CrossRef]
8. Gómez-Pacheco, C.; Sánchez-Polo, M.; Rivera-Utrilla, J.; Peñalver, J.J.L. Tetracycline removal from waters by integrated technologies based on ozonation and biodegradation. *Chem. Eng. J.* **2011**, *178*, 115–121. [CrossRef]
9. Da Silva, L.F.; M'Peko, J.-C.; Andrés, J.; Beltran, A.; Gracia, L.; Bernardi, M.I.B.; Mesquita, A.; Antonelli, E.; Moreira, M.L.; Mastelaro, V.R. Insight into the Effects of Fe Addition on the Local Structure and Electronic Properties of SrTiO3. *J. Phys. Chem. C* **2014**, *118*, 4930–4940. [CrossRef]
10. Liu, X.; Lv, P.; Yao, G.; Ma, C.; Huo, P.; Yan, Y. Microwave-assisted synthesis of selective degradation photocatalyst by surface molecular imprinting method for the degradation of tetracycline onto Cl-TiO_2. *Chem. Eng. J.* **2013**, *217*, 398–406. [CrossRef]
11. Wang, W.; Fang, J.; Shao, S.; Lai, M.; Lu, C. Compact and uniform TiO_2@g-C_3N_4 core-shell quantum heterojunction for photocatalytic degradation of tetracycline antibiotics. *Appl. Catal. B Environ.* **2017**, *217*, 57–64. [CrossRef]
12. Liu, W.; Liu, H.; Dang, L.; Zhang, X.; Wu, X.; Yang, B.; Li, Z.; Zhang, X.; Lei, L.; Jin, S. Amorphous Cobalt-Iron Hydroxide Nanosheet Electrocatalyst for Efficient Electrochemical and Photo-Electrochemical Oxygen Evolution. *Adv. Funct. Mater.* **2017**, *27*, 1603904. [CrossRef]
13. Kanan, M.W.; Nocera, D.G. In Situ Formation of an Oxygen-Evolving Catalyst in Neutral Water Containing Phosphate and Co^{2+}. *Science* **2008**, *321*, 1072–1075. [CrossRef] [PubMed]
14. Smith, R.D.L.; Prévot, M.S.; Fagan, R.D.; Trudel, S.; Berlinguette, C.P. Water Oxidation Catalysis: Electrocatalytic Response to Metal Stoichiometry in Amorphous Metal Oxide Films Containing Iron, Cobalt, and Nickel. *J. Am. Chem. Soc.* **2013**, *135*, 11580–11586. [CrossRef] [PubMed]
15. Indra, A.; Menezes, P.W.; Sahraie, N.R.; Bergmann, A.; Das, C.; Tallarida, M.; Schmeißer, D.; Strasser, P.; Driess, M. Unification of Catalytic Water Oxidation and Oxygen Reduction Reactions: Amorphous Beat Crystalline Cobalt Iron Oxides. *J. Am. Chem. Soc.* **2014**, *136*, 17530–17536. [CrossRef]
16. Kornienko, N.; Resasco, J.; Becknell, N.; Jiang, C.-M.; Liu, Y.-S.; Nie, K.; Sun, X.; Guo, J.; Leone, S.R.; Yang, P. Operando Spectroscopic Analysis of an Amorphous Cobalt Sulfide Hydrogen Evolution Electrocatalyst. *J. Am. Chem. Soc.* **2015**, *137*, 7448–7455. [CrossRef]
17. Tran, P.D.; Tran, T.V.; Orio, M.; Torelli, S.; Truong, Q.D.; Nayuki, K.; Sasaki, Y.; Chiam, S.Y.; Yi, R.; Honma, I.; et al. Coordination polymer structure and revisited hydrogen evolution catalytic mechanism for amorphous molybdenum sulfide. *Nat. Mater.* **2016**, *15*, 640–646. [CrossRef]
18. Li, H.; Chen, S.; Jia, X.; Xu, B.; Lin, H.; Yang, H.; Song, L.; Wang, X. Amorphous nickel-cobalt complexes hybridized with 1T-phase molybdenum disulfide via hydrazine-induced phase transformation for water splitting. *Nat. Commun.* **2017**, *8*, 15377. [CrossRef]
19. Lee, S.C.; Benck, J.D.; Tsai, C.; Park, J.; Koh, A.L.; Abild-Pedersen, F.; Jaramillo, T.; Sinclair, R. Chemical and Phase Evolution of Amorphous Molybdenum Sulfide Catalysts for Electrochemical Hydrogen Production. *ACS Nano* **2015**, *10*, 624–632. [CrossRef]
20. Staszak-Jirkovsky, J.; Malliakas, C.D.; Lopes, P.P.; Danilovic, N.; Kota, S.S.; Chang, K.-C.; Genorio, B.; Strmcnik, D.; Stamenkovic, V.R.; Kanatzidis, M.G.; et al. Design of active and stable Co–Mo–S_x chalcogels as pH-universal catalysts for the hydrogen evolution reaction. *Nat. Mater.* **2015**, *15*, 197–203. [CrossRef]
21. Farrow, C.L.; Bediako, D.K.; Surendranath, Y.; Nocera, D.G.; Billinge, S.J.L. Intermediate-Range Structure of Self-Assembled Cobalt-Based Oxygen-Evolving Catalyst. *J. Am. Chem. Soc.* **2013**, *135*, 6403–6406. [CrossRef] [PubMed]

22. Hu, X.L.; Piccinin, S.; Laio, A.; Fabris, S. Atomistic Structure of Cobalt-Phosphate Nanoparticles for Catalytic Water Oxidation. *ACS Nano* **2012**, *6*, 10497–10504. [CrossRef]
23. Salvatore, D.A.; Dettelbach, K.E.; Hudkins, J.R.; Berlinguette, C.P. Near-infrared–driven decomposition of metal precursors yields amorphous electrocatalytic films. *Sci. Adv.* **2015**, *1*, e1400215. [CrossRef] [PubMed]
24. Smith, R.D.L.; Prévot, M.S.; Fagan, R.D.; Zhang, Z.; Sedach, P.A.; Siu, M.K.J.; Trudel, S.; Berlinguette, C.P. Photochemical Route for Accessing Amorphous Metal Oxide Materials for Water Oxidation Catalysis. *Science* **2013**, *340*, 60–63. [CrossRef] [PubMed]
25. Zhu, J.; Lambert, F.; Policar, C.; Mavré, F.; Limoges, B. Fast magnetically driven electrodeposition of amorphous metal oxide water oxidation catalysts from carbon-coated metallic nanoparticles. *J. Mater. Chem. A* **2015**, *3*, 16190–16197. [CrossRef]
26. Kang, Y.; Yang, Y.; Yin, L.-C.; Kang, X.; Liu, G.; Cheng, H.-M. An Amorphous Carbon Nitride Photocatalyst with Greatly Extended Visible-Light-Responsive Range for Photocatalytic Hydrogen Generation. *Adv. Mater.* **2015**, *27*, 4572–4577. [CrossRef] [PubMed]
27. Rahman, M.Z.; Tapping, P.C.; Kee, T.W.; Smernik, R.; Spooner, N.; Moffatt, J.; Tang, Y.; Davey, K.; Qiao, S. A Benchmark Quantum Yield for Water Photoreduction on Amorphous Carbon Nitride. *Adv. Funct. Mater.* **2017**, *27*, 1702384. [CrossRef]
28. Zhang, R.; Li, P.; Wang, F.; Ye, L.; Gaur, A.; Huang, Z.; Zhao, Z.; Bai, Y.; Zhou, Y. Atomically dispersed Mo atoms on amorphous g-C_3N_4 promotes visible-light absorption and charge carriers transfer. *Appl. Catal. B Environ.* **2019**, *250*, 273–279. [CrossRef]
29. Han, Q.; Cheng, Z.; Wang, B.; Zhang, H.-M.; Qu, L. Significant Enhancement of Visible-Light-Driven Hydrogen Evolution by Structure Regulation of Carbon Nitrides. *ACS Nano* **2018**, *12*, 5221–5227. [CrossRef]
30. Tang, Y.; Zhou, P.; Chao, Y.; Lin, F.; Lai, J.; Li, H.; Guo, S. Face-to-face engineering of ultrathin Pd nanosheets on amorphous carbon nitride for efficient photocatalytic hydrogen production. *Sci. China Mater.* **2018**, *62*, 351–358. [CrossRef]
31. Zou, M.; Feng, L.; Pervaiz, E.; Ganeshraja, A.S.; Gao, T.; Jiang, H.; Yang, M. An Amorphous Mn, N-Codoped TiO_2 Microspheres Photocatalyst Induced by High Defects with Greatly Extended Visible-Light-Responsive Range for Photocatalytic Degradation. *Nano Adv.* **2017**, *2*, 36–44. [CrossRef]
32. Wang, J.; Xia, Y.; Zhao, H.; Wang, G.; Xiang, L.; Xu, J.; Komarneni, S. Oxygen defects-mediated Z-scheme charge separation in g-C_3N_4/ZnO photocatalysts for enhanced visible-light degradation of 4-chlorophenol and hydrogen evolution. *Appl. Catal. B Environ.* **2017**, *206*, 406–416. [CrossRef]
33. Yue, B.; Li, Q.; Iwaï, H.; Kako, T.; Ye, J. Hydrogen production using zinc-doped carbon nitride catalyst irradiated with visible light. *Sci. Technol. Adv. Mater.* **2011**, *12*, 34401. [CrossRef] [PubMed]
34. Oh, W.-D.; Chang, V.W.-C.; Hu, Z.-T.; Goei, R.; Lim, T.-T. Enhancing the catalytic activity of g-C_3N_4 through Me doping (Me = Cu, Co and Fe) for selective sulfathiazole degradation via redox-based advanced oxidation process. *Chem. Eng. J.* **2017**, *323*, 260–269. [CrossRef]
35. Li, B.; Si, Y.; Zhou, B.-X.; Fang, Q.; Li, Y.-Y.; Huang, W.-Q.; Hu, W.; Pan, A.; Fan, X.; Huang, G.-F. Doping-Induced Hydrogen-Bond Engineering in Polymeric Carbon Nitride To Significantly Boost the Photocatalytic H2 Evolution Performance. *ACS Appl. Mater. Interfaces* **2019**, *11*, 17341–17349. [CrossRef]
36. Al-Gaashani, R.; Radiman, S.; Daud, A.; Tabet, N.; Al-Douri, Y. XPS and optical studies of different morphologies of ZnO nanostructures prepared by microwave methods. *Ceram. Int.* **2013**, *39*, 2283–2292. [CrossRef]
37. Aksoy, S.; Caglar, Y.; Ilican, S.; Caglar, M. Sol–gel derived Li–Mg co-doped ZnO films: Preparation and characterization via XRD, XPS, FESEM. *J. Alloy. Compd.* **2012**, *512*, 171–178. [CrossRef]
38. Abdei-Wahab, M.S.; Jilani, A.; Yahia, I.; Alghamdi, A. Enhanced the photocatalytic activity of Ni-doped ZnO thin films: Morphological, optical and XPS analysis. *Superlattices Microstruct.* **2016**, *94*, 108–118. [CrossRef]
39. Chen, M.; Wang, X.; Yu, Y.; Pei, Z.; Bai, X.; Sun, C.; Huang, R.; Wen, L. X-ray photoelectron spectroscopy and auger electron spectroscopy studies of Al-doped ZnO films. *Appl. Surf. Sci.* **2000**, *158*, 134–140. [CrossRef]
40. Jeong, Y.; Bae, C.; Kim, D.; Song, K.; Woo, K.; Shin, H.; Cao, G.; Moon, J. Bias-Stress-Stable Solution-Processed Oxide Thin Film Transistors. *ACS Appl. Mater. Interfaces* **2010**, *2*, 611–615. [CrossRef]
41. Yu, W.; Chen, J.; Shang, T.; Chen, L.; Gu, L.; Peng, T. Direct Z-scheme g-C_3N_4/WO_3 photocatalyst with atomically defined junction for H_2 production. *Appl. Catal. B Environ.* **2017**, *219*, 693–704. [CrossRef]

42. Sun, J.-X.; Yuan, Y.; Qiu, L.-G.; Jiang, X.; Shena, Y.; Shena, Y.; Zhu, J. Fabrication of composite photocatalyst g-C_3N_4–ZnO and enhancement of photocatalytic activity under visible light. *Dalton Trans.* **2012**, *41*, 6756–6763. [CrossRef]
43. Wang, X.L.; Fang, W.Q.; Wang, H.F.; Zhang, H.; Zhao, H.; Yao, Y.; Yang, H.G. Surface hydrogen bonding can enhance photocatalytic H_2 evolution efficiency. *J. Mater. Chem. A* **2013**, *1*, 14089. [CrossRef]
44. Cao, J.; Lai, L.; Lai, B.; Yao, G.; Chen, X.; Song, L. Degradation of tetracycline by peroxymonosulfate activated with zero-valent iron: Performance, intermediates, toxicity and mechanism. *Chem. Eng. J.* **2019**, *364*, 45–56. [CrossRef]
45. Xie, Z.; Feng, Y.; Wang, F.; Chen, D.; Zhang, Q.; Zeng, Y.; Lv, W.; Liu, G. Construction of carbon dots modified MoO_3/g-C_3N_4 Z-scheme photocatalyst with enhanced visible-light photocatalytic activity for the degradation of tetracycline. *Appl. Catal. B Environ.* **2018**, *229*, 96–104. [CrossRef]
46. Panneri, S.; Ganguly, P.; Nair, H.; Mohamed, A.A.P.; Warrier, K.G.; Hareesh, U.N.S. Copyrolysed C_3N_4-Ag/ZnO Ternary Heterostructure Systems for Enhanced Adsorption and Photocatalytic Degradation of Tetracycline. *Eur. J. Inorg. Chem.* **2016**, *2016*, 5068–5076. [CrossRef]
47. Rasheed, H.U.; Lv, X.; Wei, W.; Yaseen, W.; Ullah, N.; Xie, J.; Zhu, W. Synthesis and studies of ZnO doped with g-C_3N_4 nanocomposites for the degradation of tetracycline hydrochloride under the visible light irradiation. *J. Environ. Chem. Eng.* **2019**, *7*, 103152. [CrossRef]
48. Hao, R.; Xiao, X.; Zuo, X.; Nan, J.; Zhang, W. Efficient adsorption and visible-light photocatalytic degradation of tetracycline hydrochloride using mesoporous BiOI microspheres. *J. Hazard. Mater.* **2012**, *209*, 137–145. [CrossRef]
49. Lee, K.M.; Lai, C.W.; Ngai, K.S.; Juan, J.C. Recent developments of zinc oxide based photocatalyst in water treatment technology: A review. *Water Res.* **2016**, *88*, 428–448. [CrossRef]
50. Mamba, G.; Mishra, A.K. Graphitic carbon nitride (g-C_3N_4) nanocomposites: A new and exciting generation of visible light driven photocatalysts for environmental pollution remediation. *Appl. Catal. B Environ.* **2016**, *198*, 347–377. [CrossRef]
51. Zhang, H.; Zong, R.; Zhu, Y. Photocorrosion Inhibition and Photoactivity Enhancement for Zinc Oxide via Hybridization with Monolayer Polyaniline. *J. Phys. Chem. C* **2009**, *113*, 4605–4611. [CrossRef]
52. Fu, H.; Xu, T.; Zhu, S.; Zhu, Y. Photocorrosion Inhibition and Enhancement of Photocatalytic Activity for ZnO via Hybridization with C_{60}. *Environ. Sci. Technol.* **2008**, *42*, 8064–8069. [CrossRef] [PubMed]
53. Neppolian, B. Solar/UV-induced photocatalytic degradation of three commercial textile dyes. *J. Hazard. Mater.* **2002**, *89*, 303–317. [CrossRef]
54. Wang, X.L.; Yang, H.G. Facile fabrication of high-yield graphitic carbon nitride with a large surface area using bifunctional urea for enhanced photocatalytic performance. *Appl. Catal. B Environ.* **2017**, *205*, 624–630. [CrossRef]